https://doi.org/10.1631/bdm.2300372

Received: 26 December 2023 / Accepted: 13 September 2024

RESEARCH ARTICLE

Reduced graphene oxide-mediated electron–hole separation using titanium dioxide increases the photocatalytic antibacterial activity of bone scaffolds

Pei Feng[1], Haifeng Tian[1], Feng Yang[1], Shuping Peng[2,3], Hao Pan[4,*], Cijun Shuai[1,5,6,*]

[1]State Key Laboratory of Precision Manufacturing for Extreme Service Performance, College of Mechanical and Electrical Engineering, Central South University, Changsha 410083, China

[2]NHC Key Laboratory of Carcinogenesis of Hunan Cancer Hospital and the Affiliated Cancer Hospital of Xiangya School of Medicine, Cancer Research Institute, School of Basic Medical Science, Central South University, Changsha 410013, China

[3]The Key Laboratory of Carcinogenesis and Cancer Invasion of the Chinese Ministry of Education, Xiangya Hospital, Central South University, Changsha 410078, China

[4]Department of Periodontics & Oral Mucosal Section, Xiangya Stomatological Hospital & Xiangya School of Stomatology, Central South University, Changsha 410013, China

[5]Institute of Additive Manufacturing, Jiangxi University of Science and Technology, Nanchang 330013, China

[6]College of Mechanical Engineering, Xinjiang University, Urumqi 830017, China

[*]Corresponding author: Hao Pan, panhao@csu.edu.cn; Cijun Shuai, shuai@csu.edu.cn

Abstract

Fast electron–hole recombination issues during titanium dioxide (TiO_2) photocatalysis limit its application in preventing bacterial infection during bone defect repair. In this study, TiO_2@reduced graphene oxide (rGO) composites were synthesized using a hydrothermal method in which rGO, which possesses very high electrical conductivity, promotes the separation of photoelectron–hole pairs of TiO_2, thus improving the efficiency of

photocatalytic production of reactive oxygen species (ROS). Subsequently, TiO_2@rGO composites were introduced into poly-L-lactic acid (PLLA) to prepare bone scaffolds with photocatalytic antibacterial function via selective laser sintering. The results showed that TiO_2 grew on the surface of rGO and formed a covalent bond connection (Ti–O–C) with rGO. A decreased electrochemical impedance of TiO_2@rGO composites was observed, and the transient photocurrent intensity increased from 0.05 to 0.5 μA/cm^2. Analysis of electron spin resonance found that the photocatalytic products of TiO_2 were •OH and •O_2^-, two kinds of ROS capable of killing bacteria via disrupting the structure of the bacterial membrane in vitro. Antibacterial experiments showed that the antibacterial rates of PLLA/TiO_2@rGO scaffolds against *E. coli* and *S. aureus* were 60% and 71%, respectively. Finally, we report that these scaffolds exhibited both enhanced mechanical properties due to the addition of TiO_2@rGO as a reinforcement material and good biocompatibility during cell proliferation.

Graphic abstract

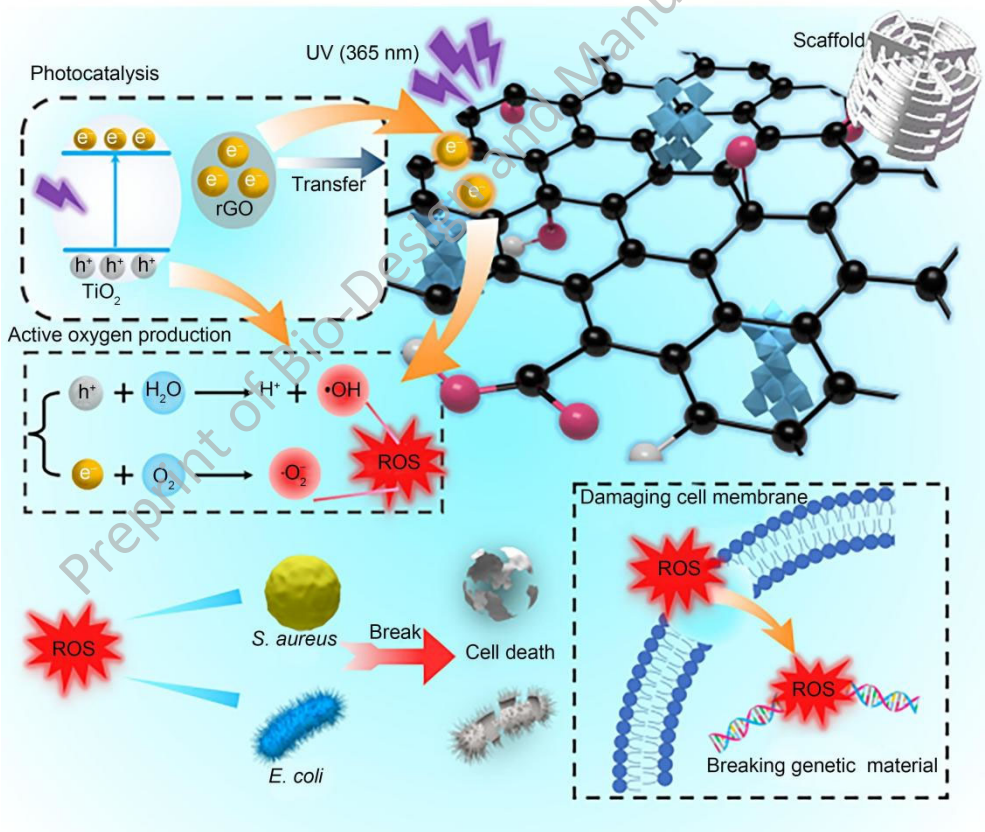

Keywords reduced graphene oxide, photocatalysis, reactive oxygen species, antibacterial properties, bone scaffold

Introduction

Bacterial infection is one of the most common complications during bone defect repair following the implantation of artificial bone scaffolds[1, 2]. The formation of bacterial biofilms on scaffolds can trigger the release of acids and enzymes, interfere with bone metabolism, destroy bone matrix, inhibit cell proliferation, and delay bone healing[3-5]. Metal oxide nanoparticles including zinc oxide (ZnO), cupric oxide (CuO), and TiO_2, among others, have been widely studied as antibacterial agents due to their ability to photocatalytically produce reactive oxygen species (ROS)[6-8], which can kill bacteria or inhibit their growth and reproduction[9-11]. TiO_2 is a metal oxide semiconductor with a wide band gap, which confers a high level of redox activity. This is because its photoelectron–hole pairs react with water (H_2O) and oxygen (O_2) in the environment to produce ROS [12-14]. However, the rapid recombination of photoelectron–hole pairs leads to low photocatalytic efficiency, thereby limiting the potential application of TiO_2.

To enhance the antibacterial efficiency of TiO_2, various methods have been used to increase the lifetime and separation efficiency of photocarriers. Such methods include changing the crystal structure and surface properties of TiO_2 to enhance its photocatalytic reaction rate and increase ROS production, thereby improving its antibacterial activity[15, 16]. For example, Alotaibi[17] et al. synthesized Cu-doped TiO_2 films via aerosol-assisted chemical vapor deposition. Their results indicated that the addition of Cu ions to TiO_2 created defects and introduced oxygen vacancies acting as traps to capture photogenerated electrons. This in turn facilitated electron–hole separation and provided redox-active sites for redox reactions. Compared with pure anatase, the resulting film exhibited strong photocatalytic activity and antibacterial ability against *Staphylococcus aureus* (*S. aureus*) and *Escherichia coli* (*E. coli*). In another study, Thukkaram[18] et al. used plasma electrolytic oxidation techniques to deposit silver (Ag) on TiO_2. Their results indicated that the high conductivity of Ag can transfer photogenerated electrons from the surface of TiO_2 to that of Ag, thereby effectively separating electrons and holes and improving its photocatalytic antibacterial ability. However, previous studies have shown that metal ions can exert certain cytotoxic effects that can inhibit cell growth and differentiation in defect areas. These effects can even kill surrounding healthy cells, thereby affecting bone defect repair[19].

Reduced graphene oxide (rGO) is a derivative of graphene, and can be obtained by

reducing graphene oxide (GO)[20, 21]. Each carbon atom in the honeycomb lattice structure of rGO forms a covalent bond with three surrounding carbon atoms. This causes the formation of a conjugated structure with π electrons that can move freely, thus giving rGO excellent conductivity[22, 23]. In one study, Zhao[24] et al. used a simple solvothermal calcination method to anchor iron vanadate Fe_2VO_4 onto rGO. They showed that highly conductive rGO accelerated the transport of electrons/ions. Since the prepared Fe_2VO_4/rGO has a large and stable antibiotic capacity, this solved the problem of low antibiotic capacity caused by the low conductivity of Fe_2VO_4. In addition, rGO retains many of the structural defects of GO, insofar as it contains oxygen functional groups and has stronger hydrophilicity than graphene, leading to less biotoxicity. However, as an intermediate between graphene and GO, rGO has both good biocompatibility and conductivity[25]. Given the results reported above, it is reasonably concluded that the excellent conductivity of rGO may promote the separation of photogenerated carriers when rGO is combined with TiO_2, thereby increasing its photocatalytic antibacterial properties.

In this study, we used tetrabutyl titanate as a precursor to successfully grow TiO_2 in situ on the surface of rGO using a hydrothermal method. During this process, GO was reduced to rGO, and TiO_2@rGO composites were prepared. Thereafter the superior electrical conductivity of rGO was utilized to promote the separation of the photogenerated electron–hole pairs of TiO_2. Next, we evaluated the chemical composition and morphology of the resulting TiO_2@rGO composites, and studied the photocatalytic mechanism and the resulting biotoxic activity. Subsequently, TiO_2@rGO composites were incorporated into poly-L-lactic acid (PLLA) powders in order to fabricate personalized scaffolds with photocatalytic antibacterial functions using a selective laser sintering (SLS) method[26-28]. The photocatalytic antibacterial properties of the scaffold were then evaluated under 365 nm ultraviolet (UV) light and dark conditions. Finally, we report the mechanical properties and biocompatibility of the resulting scaffold.

Materials and methods

Materials

Tetrabutyl titanate (purity>98.0%), hydrofluoric acid (HF, purity>40.0%), and rhodamine B (RhB, purity>99.0%) were obtained from Shanghai Aladdin Biochemical Technology Co.,

Ltd. (Shanghai, China). GO nanosheets (purity>99.9%) were purchased from Chengdu Organic Chemical Co., Ltd. (Chengdu, China). PLLA powder (purity>99.0%) was purchased from Shenzhen Polymtek Biomaterial Materials Co., Ltd. (Shenzhen, China). Finally, phosphate-buffered saline (PBS), anhydrous ethanol, and deionized water were obtained from Sinopharm Holding Chemical Reagent Co., Ltd. (Beijing, China).

Synthesis of TiO_2@rGO nanopowders

The hydrothermal method was used to synthesize composite powders. First, 150 mg GO was ultrasonically dispersed in anhydrous ethanol to obtain a 3 mg/mL GO ethanol solution. Next, tetrabutyl titanate (7 mL) and HF solution (0.8 mL) were gradually added to this solution, and then it was stirred for 10 min before reacting in a Teflon-lined reaction vessel at 150 °C for 24 h. The resulting TiO_2@rGO product was then washed twice with water, centrifuged at 6000 r/min for 10 min, and dried for 24 h. Pure TiO_2 nanoparticles were also prepared using this procedure, and the same reaction was carried out in the absence of GO.

Preparation of scaffolds

To prepare PLLA/TiO_2@rGO (PTG) composite powder, TiO_2@rGO powder was first weighed out and then dispersed ultrasonically in ethanol for 30 min. Next, PLLA powder was weighed out and mixed into a dispersing liquid before being subjected to ultrasonic dispersion for 15 min. Here, the mass ratio of PLLA to TiO_2@rGO was fixed at 19:1. After dispersion, the resulting solution was magnetically stirred for 3 h to achieve a uniformly dispersed solution[29]. After centrifuging the mixture at 6000 r/min for 8 min, the PTG composite powder was dried, ground, and collected. A PLLA/TiO_2 (PT) composite powder was prepared using the same procedure.

Next, a three-dimensional (3D) porous scaffold was prepared using an SLS system[30]. The specific steps involved in the scaffold preparation were as follows[31-33]. First, a 3D model was designed and converted into a stereolithography (STL) file, which was then imported into the SLS system so that the system could automatically calculate the bracket section data[34]. Next, a powder layer with a thickness of about 0.1 mm was evenly dispersed on a platform using a roller. A laser beam was then used to sinter the powder. This laser followed a predetermined path that was guided by the scaffold model. A laser power of 1.8 W and a scanning speed of 120 mm/s were used in the sintering process. Upon completing each

path, the platform would vertically move about the height of a single powder layer, and a new powder layer was then spread. This process was repeated systematically until the desired scaffold was obtained through layer-by-layer sintering.

Sample characterization

X-ray diffractometry (XRD) (Rigaku Ultima IV, Tokyo, Japan) was used to evaluate the crystal structures of the samples. Scans were performed with 2θ in the range of 5° to 80°, and the scanning speed was 2°/min. A Fourier transform infrared spectroscopy (FTIR) spectrometer (Thermo Scientific Nicolet iS5, Massachusetts, USA) was used to study the functional groups of the samples; scans were performed from 400 to 4000 cm^{-1}. A Raman spectrometer (Horiba LabRAM HR Evolution, Kyoto, Japan) was used to detect the sample structures at room temperature; scans were performed from 50 to 4000 cm^{-1}. Scanning electron microscopy (SEM) (Phenom-World BV, Eindhoven, the Netherlands) was used to observe the sample morphology. Images were taken after sputtering with platinum for 120 s. An X-ray photoelectron spectroscopy (XPS) spectrometer (Thermo Scientific K-Alpha, Massachusetts, USA) was used to determine the sample chemical bond binding energy. The excitation source for XPS was Al Kα ray (hv=1486.6 eV). The working voltage was 12 kV and the filament current was 6 mA. An electrochemical workstation (CHI760E, Shanghai, China) was used to test the electrochemical impedance spectroscopy and transient photocurrent responses of the samples in a three-electrode system. This system included platinum foil, as-prepared TiO_2@rGO samples, and saturated calomel electrodes as the counter, working, and reference electrodes, respectively. When testing the photocurrent intensity, the illumination interval was 20 s at an irradiation wavelength of less than 400 nm. EIS was conducted using a frequency range from 100 kHz to 0.1 Hz. A fluorescence spectrophotometer (FLS1000, Edinburgh, Britain) was used to measure the sample photoluminescence (PL) response at an excitation wavelength of 325 nm. To obtain an ultraviolet–visible (UV–vis) diffuse reflectance spectra, a UV–vis spectrophotometer (UV-3600, Shimadzu, Japan) was used to explore the sample absorbance over a range of 200–1000 nm. An electron spin resonance (ESR) spectrometer (Bruker EMX PLUS, Karlsruhe, Germany) was used to detect ROS. The detection of spin adducts was performed at ambient temperature at a microwave power of 6.325 mW, a scan range of 100 G, and a field

modulation of 1 G.

Mechanical properties

Next, the mechanical properties of the scaffold were evaluated using a mechanical testing machine (YAW-300C, Shandong, China) with the loading speed set to 0.5 mm/min. The scaffold samples used for tensile testing were dumbbell-shaped (12 mm×3 mm×3 mm), and those used for tensile and compressive testing were cylindrical (diameter 6 mm, height 10 mm). Under continuous loading, the samples fractured during tensile testing and exhibited severe deformation with 30% strain during compressive testing. These tests generated stress–strain curves that were used to calculate the modulus. Each experiment was conducted five times.

Photocatalytic activity

Next, the photocatalytic activity of the PLLA, PT, and PTG scaffolds was determined using RhB degradation. To do so, square samples (9 mm×9 mm×1 mm) were produced as sheets via SLS. PLLA, PT, and PTG scaffolds were added to three tubes that each contained 4 mL RhB solution (8 μg/mL), while a fourth tube contained no scaffold and was used as a blank control. After irradiation with UV light, we collected a sample of the supernatant every 25 min, and the absorbance of these samples was measured using a spectrophotometer (V-1800, Shanghai, China). Photocatalytic degradation curves of RhB were thereby obtained for each type of scaffold.

Antibacterial properties

To test the antibacterial activity of different scaffolds, we cultured *S. aureus* and *E. coli* in their presence and observed the microbial inhibition. To do so, both strains were first thawed from a −78 °C freezer and cultivated in autoclaved Luria-Bertani (LB) medium to get activated. Next, activated strains were streaked onto solid LB medium using an inoculating loop to obtain a single colony. This was then seeded and cultivated in LB medium at 37 °C for 1 d. The resulting bacterial suspension was then prepared for testing by dilution in sterile saline to a concentration of 1×10^8 CFU/mL. For standard bacterial plate counting assays, the initial bacterial solution was further diluted in a gradient down to as low as 1×10^6 CFU/mL. Next, samples of the PLLA, PT, and PTG scaffolds were placed in Eppendorf (EP) tubes, and 100 μL of the 1×10^6 CFU/mL bacterial solution and 900 μL LB liquid medium were

subsequently added. A separate group was cultivated without scaffolds to be used as a blank control. The bacterial solution was then irradiated with UV light (365 nm) for 30 min and incubated for 24 h. The resulting bacterial solution was diluted 1×10^5 times, and 100 μL of this solution was uniformly coated on solid LB medium. After further incubation at 37 °C for 24 h, we imaged the solid media using NIH ImageJ to obtain the colony counts. Experiments were conducted in parallel with replicates cultivated completely in the dark, serving as controls. The dark PLLA group was selected as the negative control group, while other samples were selected as experimental groups. The bacterial survival rate was then determined using the following formula[35]:

$$\text{Bacterial survival rate} = {}^{A_1}/_{A_0} \times 100\%.$$

Here, A_0 and A_1 represent the bacterial counts of the negative control and experimental groups, respectively. The antibacterial activity was then calculated as (1−bacterial survival rate).

Next, live/dead staining was used to measure the destruction of biofilms via photocatalysis. To do so, PLLA, PT, and PTG scaffolds were first placed in EP tubes, to which 100 μL bacterial solution (1×10^6 CFU/mL) and 900 μL LB liquid medium were also added. These samples were then cultivated at 37 °C for 24 h before being irradiated with UV light for 30 min. Live/dead staining was then performed using a SYTO9/PI Double Stain Kit (MKBio, MX4234, USA), and images were captured using a fluorescence microscope (Olympus IX73, Japan). Furthermore, we used SEM to assess the effect of the scaffold material on the formation of bacterial biofilms. After this experiment, scaffolds were carefully removed from the bacterial solutions, and the biofilms were washed using PBS. The cleaned biofilms were then fixed overnight at 4 °C using a 2.5% glutaraldehyde solution. Bacteria were subsequently dehydrated for 15 min before being air-dried for 24 h. Finally, all samples were characterized using SEM after sputter-coating.

Cytocompatibility

Next, we evaluated the cytocompatibility of the scaffold by assessing the proliferation status of human bone marrow stem cells (hBMSCs, American Type Culture Collection, Manassas, USA). We first created a Dulbecco's modified Eagle's culture medium that was enriched with 10% fetal bovine serum and 1% antibiotic. Next, hBMSCs were seeded onto

sterile scaffold samples at 1×10^5 cells/cm^2. Following incubation at 37 °C and 5% CO_2 for periods of 1, 3, and 7 d, we washed all samples three times with PBS, and subsequently fixed them using 2.5% glutaraldehyde at room temperature. After dehydration with graded ethanol solutions and air-drying at 35 °C, SEM was performed to observe cell adhesion to the sample surface. To evaluate the cell viability, cells were then stained using a Calcein-AM/PI Double Stain Kit (Beyotime, USA) in PBS at 37 °C for 30 min. Furthermore, a Cell Counting Kit-8 (CCK-8, Beyotime, USA) was used to assess the proliferation of hBMSCs on different scaffolds. At each evaluation time point, the medium was removed, and scaffolds were washed with PBS before being transferred to a fresh medium containing 10% CCK-8 and cultivated for an additional two hours. Next, a microplate reader (Thermo Multiskan FC, USA) was used to measure the optical density of the supernatant. Stained samples were finally visualized using a fluorescence microscope (Olympus Corporation, Tokyo, Japan); here, green fluorescence indicated living cells, while red fluorescence indicated dead cells.

Statistical analysis

All quantitative results are presented as mean±standard deviation. Statistical analysis was carried out using SPSS Version 19 (IBM SPSS, Armonk, USA). The thresholds of statistical significance were $^{*}p<0.05$ and $^{**}p<0.01$.

Results and discussion

Characterization of TiO_2@rGO

The hydrothermal method was used to synthesize the composite powder as shown in Fig. 1a. Following this procedure, SEM was used to examine the microstructure of the synthesized TiO_2 nanoparticles and TiO_2@rGO composite powder, as illustrated in Figs. 1b and 1c. Although images of the two samples appear similar, the TiO_2@rGO sample shows a pinnate two-dimensional structure, thereby illustrating a difference with respect to the TiO_2 nanoparticles. Further morphological analysis also clearly showed that the pinnate two-dimensional structure observed in TiO_2@rGO was due to the presence of rGO.

The XRD patterns of GO, synthetic TiO_2, and synthetic TiO_2@rGO are shown in Fig. 1(d). Here, the locations of the observed peaks are consistent with those found in previous reports. For example, the GO peak at 2θ=11.25° corresponds to the (001) crystal plane[36]. For TiO_2, the peak at 25.28° corresponds to the (101) crystal surface of anatase phase TiO_2, therefore

confirming that the prepared TiO_2 nanoparticles were anatase phase. Moreover, the specific diffraction peaks of TiO_2 at 2θ=37.91°, 47.86°, 53.75°, and 62.68° can be attributed to the (004), (200), (211), and (204) reflections of the TiO_2 nanocrystalline surface (JCPDS No. 21-1272), respectively[37, 38]. Taken together, these results indicate that TiO_2 nanoparticles were successfully synthesized. For TiO_2@rGO, we observed the characteristic reflection peaks that correspond to each crystal surface of anatase phase TiO_2, but also observed no specific reflection of GO; this indicates that practically all GO had been successfully reduced to rGO during the hydrothermal reaction process. Moreover, the characteristic peak of rGO was not observed, probably because its characteristic peak of about 27° is close to the (101) crystal peak of TiO_2. Next, the functional groups of GO, TiO_2, and TiO_2@rGO samples were analyzed by FTIR, as illustrated in Fig. 1(e). Here, the 3450 cm^{-1} peaks from all spectra indicated the O–H stretching vibration of the C–OH group. Next, the peak at 1627 cm^{-1} observed in GO could be attributed to C=C skeleton vibration, while the 1400 and 1087 cm^{-1} peaks corresponded to C–OH and C–O–C vibrations, respectively[38, 39]. We also observed absorption peaks at 500–800 cm^{-1} in the TiO_2 sample, which resulted from Ti–O–Ti stretching vibrations. For the TiO_2@rGO sample, a peak caused by the skeleton vibration of rGO was observed at 1627 cm^{-1}. Finally, the disappearance of a peak corresponding to C–O–C in rGO at 1087 cm^{-1} confirmed that GO was successfully reduced to rGO.

We subsequently studied the vibration modes of the three samples using Raman spectroscopy, as illustrated in Fig. 1(f). Two well-defined peaks were observed in the GO sample at 1349 and 1595 cm^{-1}, which were attributed to the D and G bands, respectively[38]. The D band, which is typical of sp^3 defects in carbon, and the G band, which has furnished valuable insight into the in-plane vibrations of sp^2-bonded carbon atoms found in graphene, were both discernible in the sample[40, 41]. Moreover, some oxygen-containing functional groups combined at the boundary of the graphite layer, resulting in a large number of defective C (sp^3) and many impurities; these collectively destroyed the graphite crystal structure. Regarding the TiO_2 sample, we observed peaks of typical anatase phases at 147 ($E_{g(1)}$), 391 (B_{1g}), 512 (A_{1g}), and 633 ($E_{g(2)}$) cm^{-1}, respectively. In addition, the TiO_2@rGO sample displayed characteristic graphene peaks, including D (1349 cm^{-1}) and G (1595 cm^{-1}) peaks, respectively. Further analysis showed a much higher strength ratio of rGO (1.21) than

that of GO (0.85), indicating that GO had been successfully converted to rGO[42]. Finally, we also observed TiO_2 peaks (i.e., at 141, 386, 506, and 634 cm^{-1}), which indicated the successful synthesis of the TiO_2@rGO composite powder.

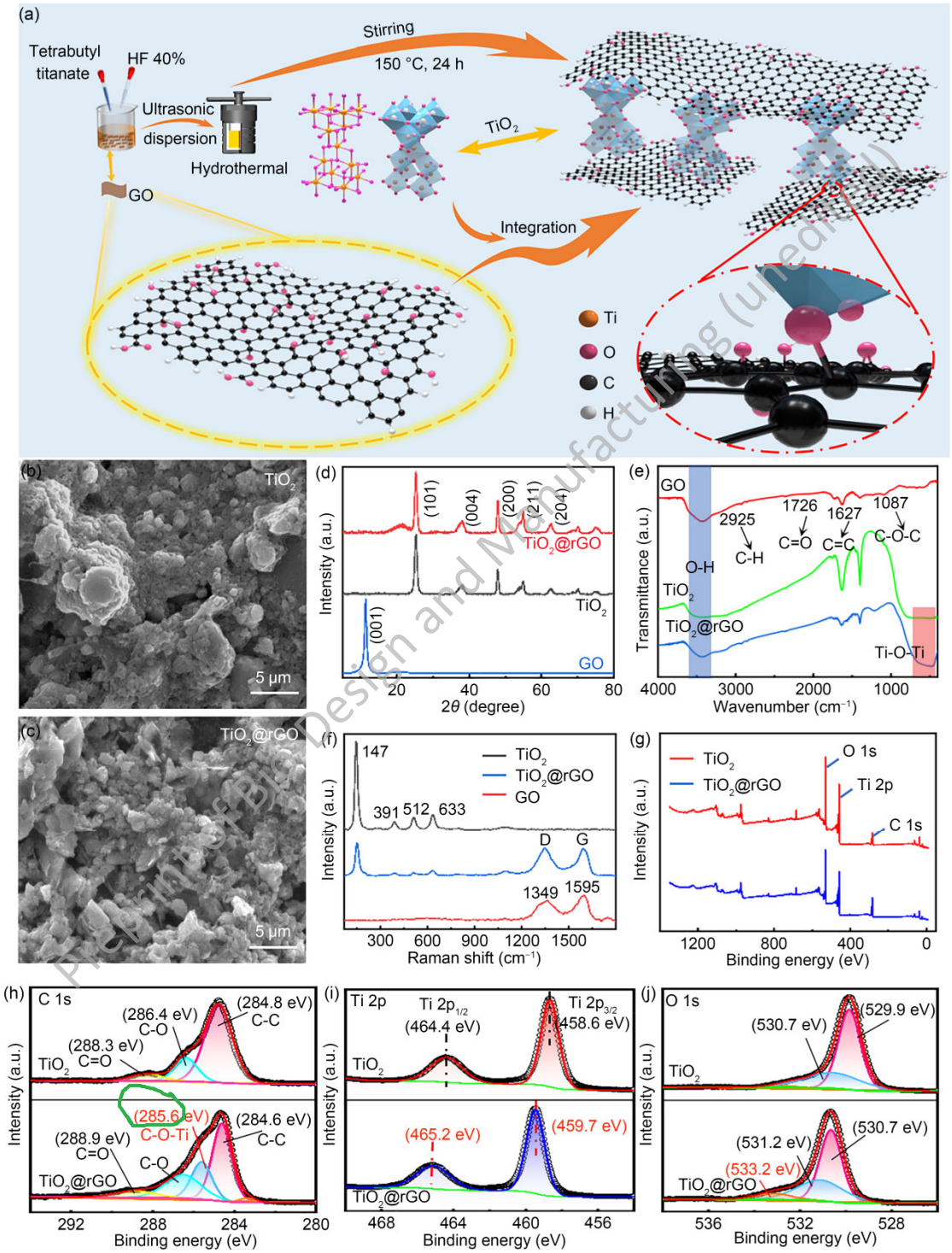

Fig. 1. (a) Schematic illustration of the preparation of TiO_2@rGO composite powder by hydrothermal method. SEM morphologies of (b) TiO_2 and (c) TiO_2@rGO. (d) The XRD

spectra, (e) FTIR spectra, and (f) Raman spectra of TiO_2 and TiO_2@rGO powders. The XPS investigation: (g) wide-scan survey, (h) C 1s spectra, (i) Ti 2p spectra, and (j) O 1s spectra of TiO_2 and TiO_2@rGO powders. TiO2: titanium dioxide; rGO: reduced graphene oxide; SEM: scanning electron microscopy; XRD: X-ray diffractometry; FTIR: Fourier transform infrared spectroscopy; XPS: X-ray photoelectron spectroscopy; HF: hydrofluoric acid

Next, we conducted XPS to analyze the composition of TiO_2 and TiO_2@rGO samples. Analysis of the obtained spectra revealed the existence of O, Ti, and C, and these outcomes are presented in Fig. 1(g). Next, the high-resolution XPS spectra of C, Ti, and O were analyzed and the results are displayed in Figs. 1(h)–1(j). The C 1s binding energy peaks measured in the TiO_2 sample were at 284.8 eV (C–C), 286.4 eV (C–O), and 288.3 eV (C=O), while equivalent measurements for the TiO_2@rGO sample were 284.6, 286.5, and 288.9 eV, respectively[38]. However, an additional binding energy peak located at 285.6 eV was observed in the TiO_2@rGO sample. Combined with the above characterization experiments, this was found to be a C–O–Ti bond, indicating that TiO_2 and rGO had chemically bonded. This change is advantageous for facilitating the transfer of photogenerated charge carriers. Furthermore, the binding energies of Ti $2p^{1/2}$ and Ti $2p^{3/2}$ in TiO_2 were 464.4 and 458.6 eV, respectively, while those of the TiO_2@rGO had changed to 465.2 and 459.7 eV, respectively. This difference is indicative of electron transfer from TiO_2 to rGO, leading to an increase in TiO_2 binding energy. As shown in Fig. 1(j), the binding energies of O 1s in the TiO_2 sample were at 529.9 eV (Ti–O bond) and 530.7 eV (C–O bond), while the binding energy peaks of the TiO_2@rGO sample had changed to 530.7 eV (Ti–O bond) and 531.2 eV (C–O bond). We also observed a C=O bond at 533.2 eV. Next, XPS results confirmed that a bond was established between TiO_2 and rGO, which promoted electron transfer. Taken together, our results indicate the successful adhesion of TiO_2 nanoparticles on rGO, as well as the successful synthesis of TiO_2@rGO, which in turn was conducive to the transfer of photogenerated carriers during photocatalytic reactions. Previous studies have indicated that the migration of photogenerated carriers was crucial for the photocatalytic production of ROS[43].

We subsequently investigated and characterized the photocatalytic activity of these two samples. We first measured their light absorption characteristics using ultraviolet–visible

(UV–vis) spectroscopy, as illustrated in Fig. 2(a). The absorption band edge of the TiO_2 sample was around 390 nm, which was similar to that of TiO_2@rGO and was consistent with previously reported results[44]. rGO did not significantly broaden the optical response range of TiO_2. Subsequently, we characterized photocatalytic activity under UV light at 365 nm. The effect of rGO on photogenerated electron–hole pair separation was demonstrated by transient photocurrent response and electrochemical impedance spectroscopy (EIS) measurements[45, 46]. An equivalent circuit diagram was obtained via EIS measurement and is shown in Fig. 2(b), with measured results presented in Fig. 2(c). The diameter of the Nyquist circle was positively correlated with the magnitude of electrochemical impedance[45, 47]. Here, we found that the TiO_2@rGO sample exhibited a shorter Nyquist circle diameter than the TiO_2 sample, indicating that it showed a much smaller interfacial charge transfer resistance and a better charge transfer efficiency.

The efficiency of the separation and conversion of photogenerated carriers in the presence of the photocatalyst was then studied using a series of experiments. PL is an effective technique for evaluating the efficiency of electron–hole separation[45, 48]. When a photocatalyst absorbs light energy to produce photogenerated carriers, the subsequent recombination of charge carriers results in the emission of light. Generally, the PL intensity is directly proportional to the degree of the photogenerated electron–hole pair separation. Thus, higher carrier separation efficiency causes lower PL intensity, resulting in more efficient photocatalytic behavior. Here, the PL spectra of the two samples at atmospheric temperature under a 365 nm UV light are presented in Fig. 2(d). These data feature a broad emission peak centered at 435 nm. Moreover, the higher PL strength of TiO_2 indicates that the holes and electrons of TiO_2 were easier to recombine, thereby confirming that the addition of rGO is conducive to the inhibition of carrier recombination[49].

Transient photocurrent responses related to interfacial charge separation were then studied by collecting multiple switching cycles under a 365 nm UV light, as shown in Fig. 2(e). In general, a higher photon-producing carrier separation rate supports greater photocatalytic efficiency. Moreover, the stronger the index of photocurrent intensity, the higher the photocatalytic efficiency and activity. As illustrated in Fig. 2(f), we found that the photocurrent density increased when the power was turned on and the illumination begun, and

decreased in the dark. Moreover, the relatively higher photocurrent intensity observed in TiO_2@rGO compared to TiO_2 suggested that rGO effectively enhanced the separation efficiency of photogenerated carriers[50]. In addition, as shown in Figs. 2(g)–2(i), ESR was used to detect ROS produced by TiO_2@rGO under photocatalytic conditions. The •OH signal was the strongest, followed by $•O_2^-$. In contrast, we observed almost no signal for $^1O_2$[45]. These data indicate that •OH was the main product of TiO_2@rGO photocatalysis, while a small amount of $•O_2^-$ was also produced. Collectively, these were the main factors contributing to photocatalytic antibacterial activity.

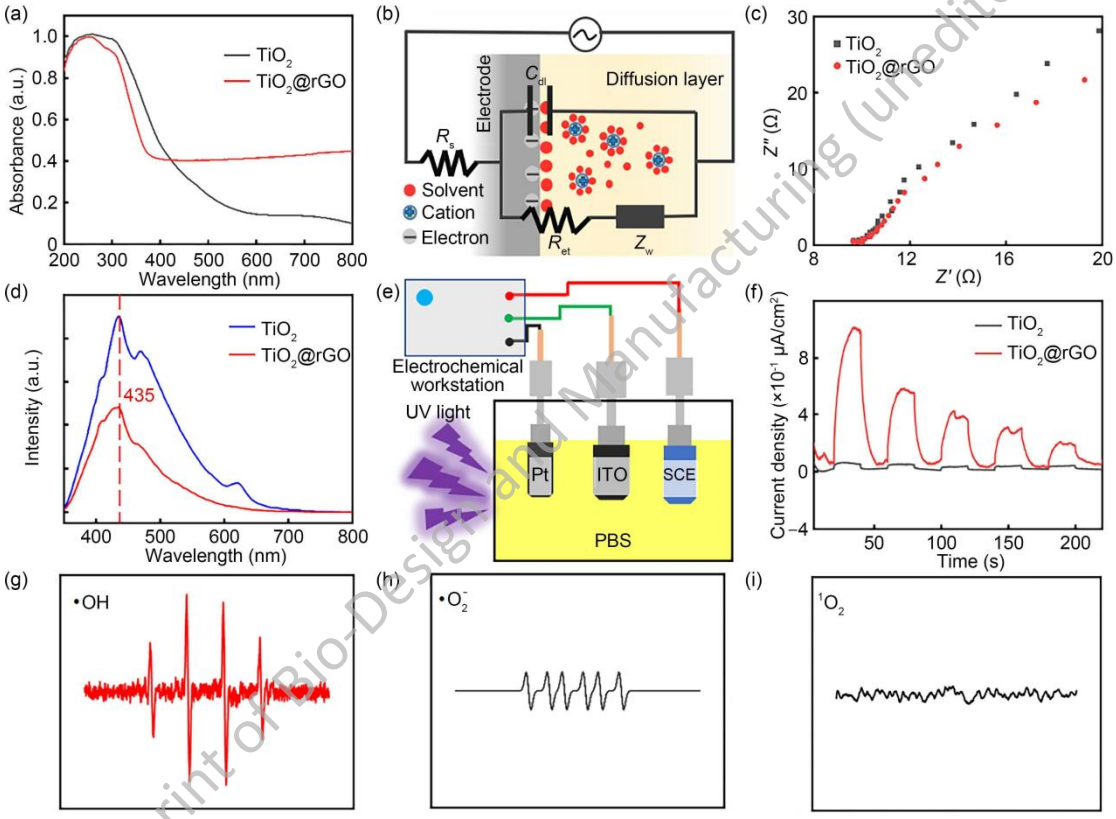

Fig. 2. Photocatalytic study of TiO_2 and TiO_2@rGO: (a) UV–vis diffuse reflectance spectra of TiO_2 and TiO_2@rGO; (b) equivalence circuit diagram and (c) results of electrochemical impedance measurement of TiO_2 and TiO_2@rGO; (d) PL spectra of TiO_2 and TiO_2@rGO; (e) installation diagram and (f) results of transient photocurrent test; electron spin resonance for (g) •OH, (h) $•O_2^-$, and (i) $^1O_2$ generation after TiO_2@rGO powders were induced by UV. TiO_2: titanium dioxide; rGO: reduced graphene oxide; UV–vis: ultraviolet–visible; PL: photoluminescence; Pt: platinum; ITO: indium tin oxide; SCE: saturated calomel electrode

Scaffold characteristics

Next, we produced scaffolds and examined their properties. First, PLLA powder and the prepared PT and PTG composite powders were processed into scaffolds with personalized porous structures using the SLS technique, as shown in Fig. 3(a). The design of the porous support is shown in Fig. 3(b). In general, the scaffold was cylindrical (diameter 12 mm, height 12.5 mm) and had a number of through-holes distributed on its upper front portion, as well as a large number of lateral holes[51, 52]. These features were implemented because they facilitate nutrient delivery and cell proliferation[53, 54]. Next, FTIR and XRD were used to analyze the scaffold composition, and the results are illustrated in Figs. 3(c) and 3(d), respectively. FTIR spectra for PTG show a peak at 500–800 cm^{-1} that indicates the presence of TiO_2. Similarly, in the XRD patterns, a peak observed at 2θ=25.3° for the PT and PTG samples confirmed the presence of TiO_2 in the scaffolds. Collectively, the FTIR and XRD data affirm that the scaffolds were successfully prepared.

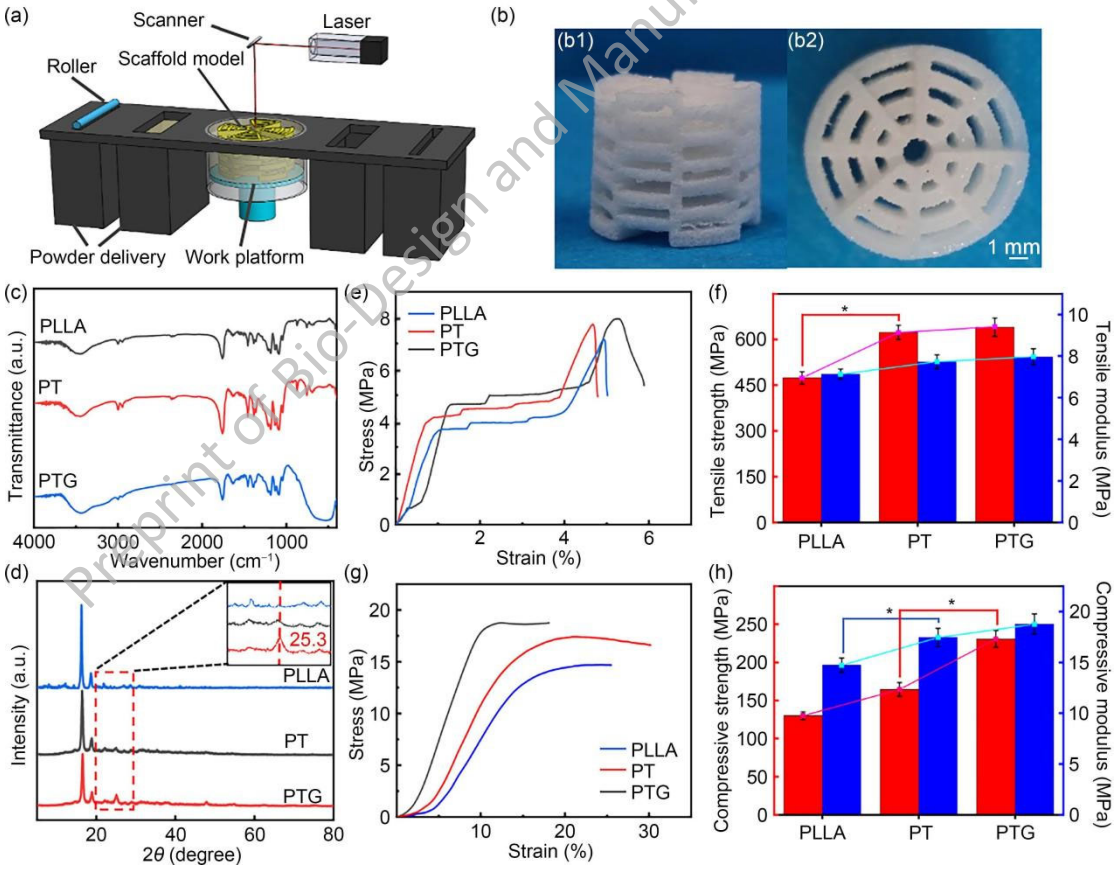

Fig. 3. (a) Schematic illustration of the SLS procession. (b) Digital images of the scaffold: (b1) side view; (b2) top view. (c) The XRD spectra and (d) FTIR spectra of PLLA, PT, and PTG

scaffold samples. (e) Tensile stress–strain curves and (f) tensile strength and modulus of the scaffolds. (g) Compressive stress–strain curves and (h) compressive strength and modulus of the scaffolds. Data are expressed in mean±standard deviation, n=5, $^{*}p$<0.05. SLS: selective laser sintering; XRD: X-ray diffractometry; FTIR: Fourier transform infrared spectroscopy; PLLA: poly-L-lactic acid; TiO_2: titanium dioxide; rGO: reduced graphene oxide; PT: PLLA/TiO_2; PTG: PLLA/TiO_2@rGO

Next, we evaluated the mechanical properties of the PLLA, PT, and PTG scaffolds using tensile and compressive tests; the results are shown in Figs. 3(e)–3(h). Overall, both the scaffold containing TiO_2 and that containing TiO_2@rGO exhibited improved tensile strength and modulus. Specifically, the PTG scaffold demonstrated a notable increase in tensile strength from 474 to 640 MPa relative to the PLLA scaffold, while its modulus was only slightly higher. Moreover, we also observed greater compressive strength and modulus of both the scaffold containing TiO_2 and that containing TiO_2@rGO. Specifically, the PTG scaffold showed increased compressive strength—i.e., from 130 to 230 MPa—and an increase in compressive modulus from 14.73 to 18.77 MPa, resulting in 76.9% and 27.4% improvement, respectively, relative to the PLLA scaffold. Taken together, these results show that incorporating TiO_2 and TiO_2@rGO as reinforcement phases resulted in improved mechanical properties with respect to the PLLA scaffold.

Photocatalytic activity of scaffolds

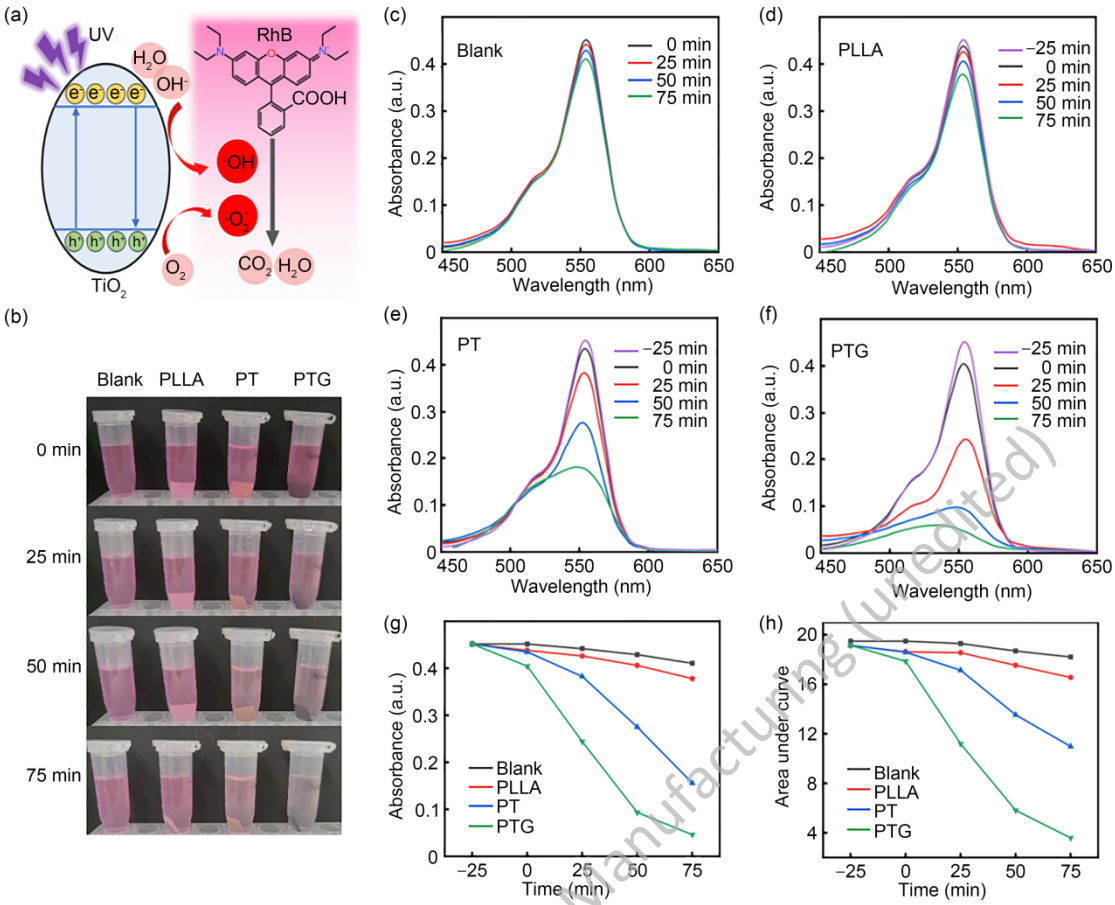

Fig. 4. (a) Schematic diagram of photocatalytic degradation of RhB. (b) Digital images of RhB degradation by PLLA, PT and PTG scaffolds photocatalysis under UV irradiation for different times (0, 25, 50 and 75 min). (c)-(f) Absorption curves of RhB degradation by blank, PLLA, PT and PTG scaffolds photocatalysis under UV irradiation, respectively. (g) Trends in the absorbance peaks of the RhB curves at each UV exposure time point. (h) Areas under the absorption curves at each time point. RhB: rhodamine B; PLLA: poly-L-lactic acid; TiO_2: titanium dioxide; rGO: reduced graphene oxide; PT: PLLA/TiO_2; PTG: PLLA/TiO_2@rGO; UV: ultraviolet

The photocatalytic activities of the PLLA, PT, and PTG scaffolds were determined by the RhB degradation method, as shown in Fig. 4(a). RhB belongs to the xanthene dye family, which can be degraded by photobleaching and N-desulfurization via TiO_2 photocatalysis[55, 56]. The PLLA, PT, and PTG scaffolds were then submerged in RhB solution and irradiated with UV light to observe the color fading of the solution; the results are shown in Fig. 4(b). The absorbance of the solution at different time points was measured using a visible

spectrophotometer over a wavelength range of 450–650 nm, as illustrated in Figs. 4(c)–4(f). The color of the RhB solution with the PTG scaffold became lighter, and the absorbance decreased after 75 min of UV irradiation[48]. The absorption curves of the PLLA scaffold and blank control groups remained basically unchanged, indicating that the PTG scaffold produced ROS and degraded RhB under UV irradiation. The same trend was observed for the PT scaffold, but to a lesser extent. Next, we analyzed changes in the absorption peak, and the area under the curves was analyzed, as illustrated in Figs. 4(g) and 4(h). The PTG scaffold had the fastest degradation rate, and the highest degree of RhB degradation under UV irradiation, which resulted from the ability of rGO to separate electron holes and improve the photocatalytic efficiency of TiO_2.

In vitro photocatalytic antibacterial effect

To investigate the antibacterial ability of the PLLA, PT, and PTG scaffolds, we conducted in vitro antibacterial experiments. The impact of the scaffolds on the proliferation of *E. coli* and *S. aureus* was observed by differences in bacterial populations cultivated on Petri dishes, as shown in Figs. 5(a) and 5(b). Taking the PLLA scaffold in dark conditions as a negative control group, the number of bacterial colonies on the PT scaffold decreased slightly, while the number present on the PTG scaffold decreased significantly. This indicated that TiO_2 exerted a photocatalytic antibacterial effect, and that the addition of rGO effectively improved this effect. Since biofilm formation is a crucial factor for implant-associated infections, we then examined the ability of the scaffolds to eliminate biofilms. A live/dead staining experiment of bacterial biofilms treated by photocatalysis showed that UV irradiation of the PTG scaffold exerted a strong destructive effect on bacterial biofilms, as illustrated in Figs. 5(c) and 5(d). However, only a small amount of the bacterial biofilm was destroyed by UV irradiation alone. Next, we obtained bacterial counts of each group using plate counting experiments and used this information to calculate survival rates, as shown in Figs. 5(e) and 5(f). Under dark conditions, both the PT and PTG scaffolds had a weak inhibitory effect against bacteria due to the presence of TiO_2 and rGO. Compared to dark conditions, UV

irradiation led to a slight decrease in the survival rates of both bacterial strains. However, exposure to UV irradiation in the presence of the PTG scaffold exhibited a considerable reduction in bacterial survival rate, with *E. coli* and *S. aureus* displaying survival rates of 40% and 29%, respectively, compared to survival rates of 62% and 45% for *E. coli* and *S. aureus* in the PT scaffold. This indicated that the presence of rGO enhanced the photocatalytic activity of TiO_2 with respect to ROS production, thereby enhancing the antibacterial effect.

However, we also note that the antibacterial effect was not ideal, possibly due to the weak penetration ability of UV light. This may have been an issue since the antibacterial substances were encapsulated in PLLA, making them difficult to release[42]. In the future, new research should use certain methods to promote the release of antibacterial substances. These may include enhancing the degradation rate of the scaffold or shifting the absorption range of TiO_2 toward longer wavelengths to improve its photocatalytic efficiency.

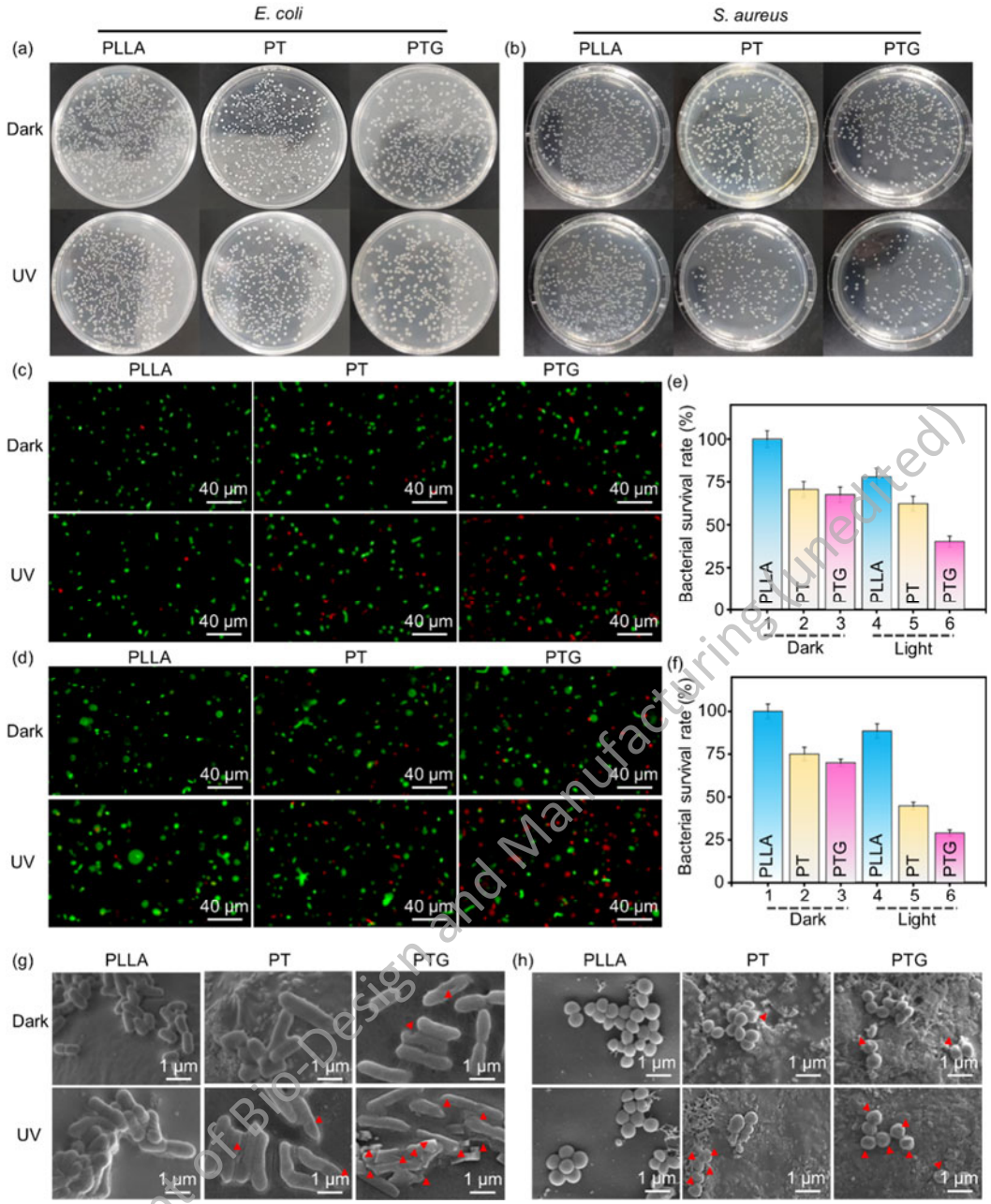

Fig. 5. Photographs of (a) *E. coli* and (b) *S. aureus* colonies after various treatments of PLLA, PT, and PTG scaffolds, respectively, under dark conditions (above) and UV light exposure for 30 min (below). Typical fluorescence images of live and dead (c) *E. coli* colonies and (d) *S. aureus* cells after various treatments of PLLA, PT, and PTG scaffolds, respectively, under dark conditions (above) and UV light exposure for 30 min (below). Bacterial survival rate of (e) *E. coli* and (f) *S. aureus*. SEM images of (g) *E. coli* colony and (h) *S. aureus* cell biofilms on the scaffolds; red arrowheads indicate holes on the bacterial surface. *E. coli*: *Escherichia coli*; *S. aureus*: *Staphylococcus aureus*; PLLA: poly-L-lactic acid; TiO_2: titanium dioxide; rGO: reduced graphene oxide; PT:

PLLA/TiO_2; PTG: PLLA/TiO_2@rGO; UV: ultraviolet; SEM: scanning electron microscopy

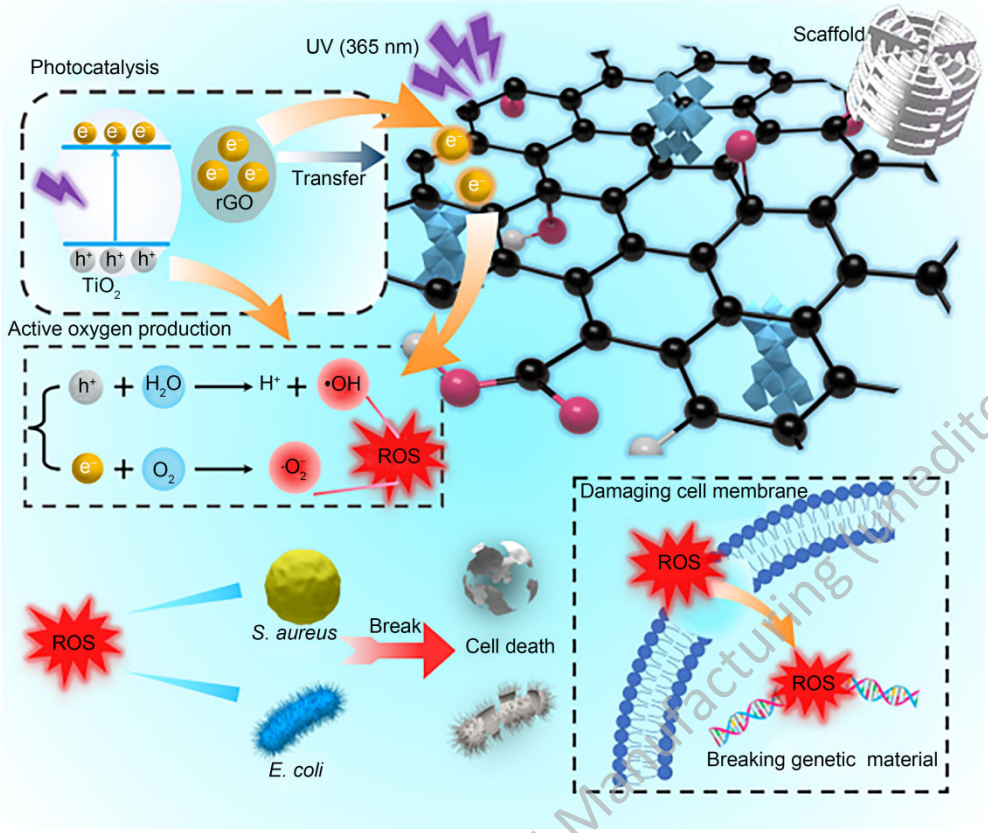

Fig. 6. Schematic illustration of antibacterial mechanism of the PTG scaffold under UV light irradiation. PLLA: poly-L-lactic acid; TiO_2: titanium dioxide; rGO: reduced graphene oxide; PTG: PLLA/TiO_2@rGO; UV: ultraviolet

Next, the morphological changes of the bacteria on the PLLA, PT, and PTG scaffolds both without and under UV irradiation were studied by SEM characterization, as shown in Figs. 5(g) and 5(h). In the control group, untreated *E. coli* and *S. aureus* exhibited smooth and intact cell walls. Furthermore, in all of the unilluminated groups, bacterial morphology remained almost unchanged. However, when the PT scaffold was irradiated with UV light, several bacteria were damaged, and their surfaces became wrinkled. In further contrast was the PTG scaffold, which caused serious damage to the bacteria after UV irradiation, resulting in unclear bacterial boundaries, different degrees of surface depression, and damage to the bacterial cell wall. Taken together, these results demonstrate that the PTG scaffold can destroy existing biofilms and prevent biofilm formation under UV irradiation. Moreover, the photocatalytic antibacterial mechanisms of the PTG scaffold are shown in Fig. 6[57]. Notably, the PTG scaffold contained TiO_2@rGO, and electrons in the valence band of TiO_2 absorbed

photon energy that could be then transferred to the conduction band for activation, resulting in the production of holes in the valence band in response to UV light irradiation. Furthermore, due to the superior electrical properties of rGO, the electrons in the conduction band were readily transferred to the rGO surface, thereby preventing the recombination of the electrons and holes[58, 59]. This caused oxidation-reducing reactions, with the electrons and holes reacting with H_2O and O_2 in the environment, respectively, which produced ROS including •OH and $•O_2^-$. These ROS oxidized bacterial membrane structures, leading to fractures, and destroyed the bacterial genetic material to achieve scaffold photocatalysis-based antibacterial effects.

Cytocompatibility

Next, cell assays were conducted to assess the biocompatibility of the PTG scaffold, with the PLLA scaffold serving as the control. Figure 7(a) depicts the SEM images of hBMSCs cultured on these scaffolds for 1, 3, and 7 d. After 1 d, hBMSCs on the PLLA scaffold exhibited a slim spindle shape and had distinctly separated from one another. Some filamentous pseudopodia extensions were observed on the PTG scaffold. After 3 d, the cell coverage area increased and an irregular polygonal shape emerged as filamentous extensions intermingled. After 7 d, hBMSCs had grown and extended on the PTG scaffold to form a cell layer. We suggest that the PTG scaffold may have better cytocompatibility, indicating that the addition of rGO and TiO_2 to the PLLA scaffold could promote cell adhesion[60, 61].

Next, the cell viability for both the PLLA and PTG scaffolds was assessed via fluorescent staining techniques to distinguish living (green) and dead (red) cells, as illustrated in Fig. 7(b). From these images, it is obvious that living cells spread well and increased in number over time, since the filamentous pseudopodia grew and we observed few dead cells on the scaffolds. In addition, we observed that the PTG scaffold showed higher cell viability than the PLLA scaffold at each sampling time; this observation was consistent with the results of the cell adhesion experiment. We suggest that TiO_2@rGO can promote cell proliferation on PLLA. In addition, the cell relative area, cell density, and CCK-8 result of each group were statistically analyzed and calculated, as shown in Figs. 7(c)–7(e). The superior ability of the PTG scaffold to promote hBMSC growth may be attributed to several factors[62]. First, the incorporation of TiO_2@rGO improved the scaffold hydrophilicity, which facilitated cell

adhesion and proliferation[63, 64]. Second, the large, rough surface area of TiO_2@rGO offered more sites for cell adhesion, and the presence of Ti helped to stimulate cell growth.

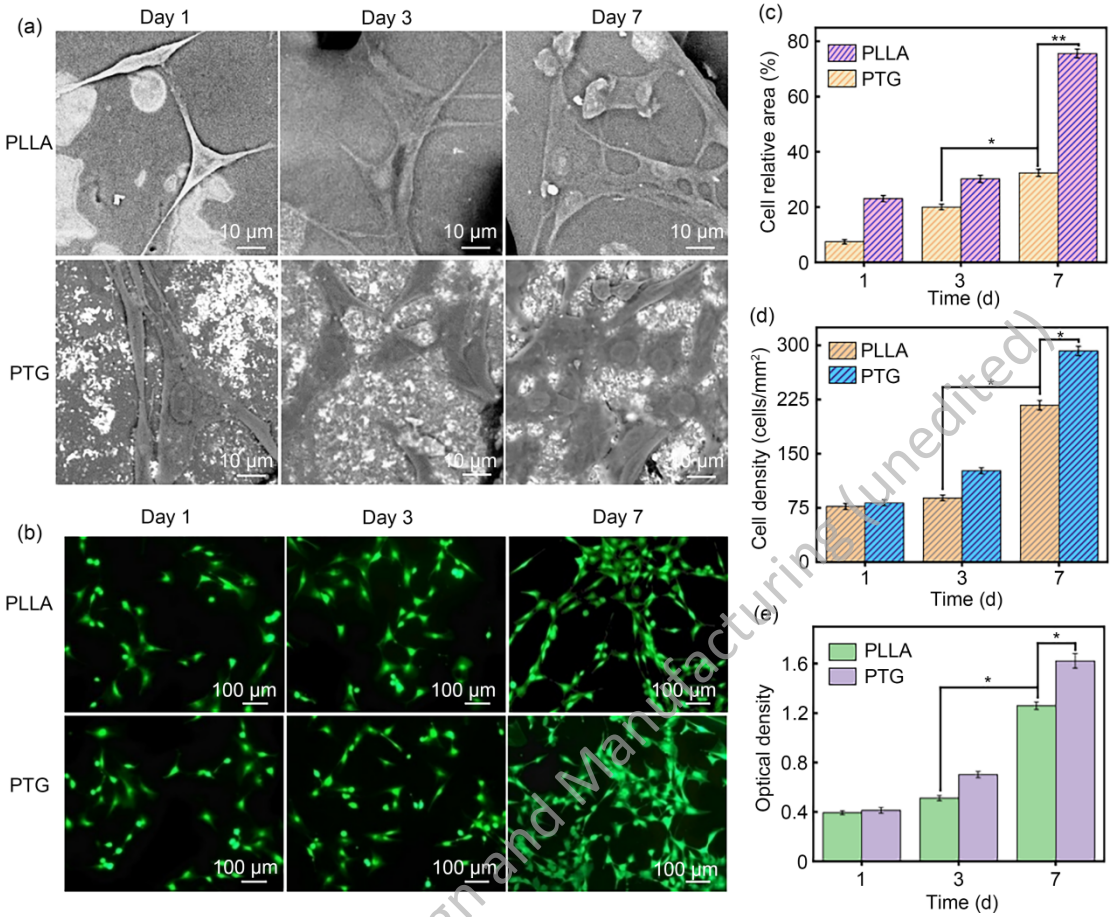

Fig. 7. (a) hBMSC morphologies cultured on the PLLA and PTG scaffolds for 1, 3, and 7 d. (b) Fluorescence staining images of the PLLA and PTG scaffolds for 1, 3, and 7 d. The corresponding statistical analysis of (c) cell relative area and (d) cell density. (e) The CCK-8 results of cells cultured on the PLLA and PTG scaffolds for 1, 3, and 7 d at a wavelength of 450 nm. Data are expressed in mean±standard deviation, n=3, $^{*}p$<0.05,$^{**}p$<0.01. hBMSC: human bone marrow stem cell; PLLA: poly-L-lactic acid; TiO_2: titanium dioxide; rGO: reduced graphene oxide; PTG: PLLA/TiO_2@rGO; CCK-8: Cell Counting Kit-8

Conclusions

In summary, in this paper we report that TiO_2@rGO composites were created using the hydrothermal method and were introduced into PLLA, and photocatalytic antibacterial bone scaffolds were prepared using SLS. After UV irradiation, the free electrons in the conduction band of TiO_2 transferred to the surface of rGO, avoiding recombination with holes, which was found to improve the photocatalytic activity of TiO_2. In general, the main photocatalytic

products of TiO_2@rGO were •OH and $•O_2^-$. Compared to the PT scaffold, the PTG scaffold showed improved antibacterial properties as measured by comparing antibacterial rates against *E. coli* and *S. aureus* (i.e., 60% and 71%, respectively). In addition, the incorporation of TiO_2@rGO improved the mechanical properties and biocompatibility of the scaffold. This study provides a feasible strategy for the antibacterial functionalization of bone scaffolds and expands potential antibacterial applications of TiO_2.

Author contributions

PF, HFT, and CJS produced the original idea. PF, HFT, and FY designed the experiment. HFT, FY, SPP, and HP performed the experimental synthesis and characterizations. PF, HFT, FY, SPP, HP, and CJS discussed the results and analyzed the experimental data. PF and HFT revised the manuscript. All authors read and approved the final manuscript.

Acknowledgements

This work was supported by the following funds: (1) The Natural Science Foundation of China (Nos. 52275393, 51935014, and 82072084); (2) Jiangxi Provincial Natural Science Foundation of China (No. 20224ACB204013); (3) The Project of State Key Laboratory of Precision Manufacturing for Extreme Service Performance; (4) the National Key Research and Development Program of China (Grant No. 2023YFB4605800); and (5) the Independent Exploration and Innovation Project of Central South University (No. 1053320221707). The authors also thank Shiyanjia Lab (www.shiyanjia.com) for the electron spin resonance measurements.

Declarations

Conflict of interest The authors declare that they have no conflict of interest.

Ethical approval This article does not contain any studies with human or animal subjects performed by any of the authors.

References

1. Wu YZ, Liao Q, Wu L et al (2021) ZnI_2-BPs integrated bone scaffold under sequential photothermal mediation: a win–win strategy delivering antibacterial therapy and fostering osteogenesis thereafter. ACS Nano 15(11):17854-17869.

https://doi.org/10.1021/acsnano.1c06062

2. Shuai CJ, Shi XX, Wang K et al (2024) Ag-doped CNT/HAP nanohybrids in a plla bone scaffold show significant antibacterial activity. Bio-Des Manuf 7(2):105-120. https://doi.org/10.1007/s42242-023-00264-0
3. Qi GB, Zhang D, Liu FH et al (2017) An “on-site transformation” strategy for treatment of bacterial infection. Adv Mater 29(36):1703461. https://doi.org/10.1002/adma.201703461
4. Zhao CQ, Liu WY, Zhu M et al (2022) Bioceramic-based scaffolds with antibacterial function for bone tissue engineering: a review. Bioact Mater 18:383-398. https://doi.org/10.1016/j.bioactmat.2022.02.010
5. Cheng H, Wang JM, Yang YQ et al (2022) Ti_3C_2TX mxene modified with ZnTCPP with bacteria capturing capability and enhanced visible light photocatalytic antibacterial activity. Small 18(26):e2200857. https://doi.org/10.1002/smll.202200857
6. Chen DJ, Cheng YL, Zhou N et al (2020) Photocatalytic degradation of organic pollutants using TiO_2-based photocatalysts: a review. J Clean Prod 268:121725. https://doi.org/10.1016/j.jclepro.2020.121725
7. Shuai CJ, Shi XX, Yang F et al (2023) Oxygen vacancy boosting fenton reaction in bone scaffold towards fighting bacterial infection. Int J Extrem Manuf 6(1):015101. https://doi.org/10.1088/2631-7990/ad01fd
8. Shuai CJ, Xie JD, Jiang XH et al (2024) Additively manufactured high entropy alloy with high wear resistance for biomedical implant. Vacuum 221:112939. https://doi.org/10.1016/j.vacuum.2023.112939
9. Wu WF, Qin YN, Fang Y et al (2023) Based on multi-omics technology study the antibacterial mechanisms of pH-dependent N-GQDs beyond ROS. J Hazard Mater 441:129954. https://doi.org/10.1016/j.jhazmat.2022.129954
10. Shuai CJ, Wang KD, Peng SP et al (2024) Accelerating Ce^{3+}/Ce^{4+} conversion in CeO_2 via Mn doping to endow scaffolds with chemodynamic therapy properties. Surf Interfaces 45:103846. https://doi.org/10.1016/j.surfin.2024.103846
11. Ran B, Ran L, Hou JG et al (2022) Incorporating boron into niobic acid nanosheets enables generation of multiple reactive oxygen species for superior antibacterial action. Small 18(17):e2107333. https://doi.org/10.1002/smll.202107333

12. Arun J, Nachiappan S, Rangarajan G et al (2023) Synthesis and application of titanium dioxide photocatalysis for energy, decontamination and viral disinfection: a review. Environ Chem Lett 21(1):339-362. https://doi.org/10.1007/s10311-022-01503-z
13. Hunge YM, Yadav AA, Khan S et al (2021) Photocatalytic degradation of bisphenol a using titanium dioxide@ nanodiamond composites under UV light illumination. J Colloid Interf Sci 582:1058-1066. https://doi.org/10.1016/j.jcis.2020.08.102
14. Liang Y, Huang GH, Xin XY et al (2022) Black titanium dioxide nanomaterials for photocatalytic removal of pollutants: a review. J Mater Sci Technol 112:239-262. https://doi.org/10.1016/j.jmst.2021.09.057
15. Shuai CJ, Zhang J, Yang YW et al (2024) Epitaxial growth of rare-earth yttrium on nanosheets to form semicoherent interface in zinc implant. J Mater Res Technol 29:1206-1217. https://doi.org/10.1016/j.jmrt.2024.01.203
16. Li YP, Shu SX, Huang LY et al (2023) Construction of a novel double s-scheme structure WO_3/g-C_3N_4/BiOI: enhanced photocatalytic performance for antibacterial activity. J Colloid Interf Sci 633:60-71. https://doi.org/10.1016/j.jcis.2022.11.058
17. Alotaibi AM, Williamson BAD, Sathasivam S et al (2020) Enhanced photocatalytic and antibacterial ability of Cu-doped anatase TiO_2 thin films: theory and experiment. ACS Appl Mater Interfaces 12(13):15348-15361. https://doi.org/10.1021/acsami.9b22056
18. Thukkaram M, Cools P, Nikiforov A et al (2020) Antibacterial activity of a porous silver doped TiO_2 coating on titanium substrates synthesized by plasma electrolytic oxidation. Appl Surf Sci 500:144235. https://doi.org/10.1016/j.apsusc.2019.144235
19. Chhipa H, Srinivasa Reddy T, Soni SK et al (2020) Self-assembled nanostructures of phosphomolybdate, nucleobase and metal ions synthesis and their in vitro cytotoxicity studies on cancer cell lines. J Mater Chem B 8(48):11044-11054. https://doi.org/10.1039/D0TB01945C
20. Tarcan R, Todor-Boer O, Petrovai I et al (2020) Reduced graphene oxide today. J Mater Chem C 8(4):1198-1224. https://doi.org/10.1039/C9TC04916A
21. Qi FW, Li HX, Gao XW et al (2024) Oxygen vacancy healing boosts the piezoelectricity of bone scaffolds. Biomater Sci-UK 12(2):495-506. https://doi.org/10.1039/D3BM01283B

22. Wang YL, Chen YN, Lacey SD et al (2018) Reduced graphene oxide film with record-high conductivity and mobility. Mater Today 21(2):186-192. https://doi.org/10.1016/j.mattod.2017.10.008
23. Song JN, Zhang Y (2020) Vertically aligned silicon carbide nanowires/reduced graphene oxide networks for enhancing the thermal conductivity of silicone rubber composites. Compos Part A-Appl S 133:105873. https://doi.org/10.1016/j.compositesa.2020.105873
24. Zhao DC, Zhang Z, Ren JH et al (2023) Fe_2VO_4 nanoparticles on rGO as anode material for high-rate and durable lithium and sodium ion batteries. Chem Eng J 451:138882. https://doi.org/10.1016/j.cej.2022.138882
25. Narayanan KB, Kim HD, Han SS (2020) Biocompatibility and hemocompatibility of hydrothermally derived reduced graphene oxide using soluble starch as a reducing agent. Colloid Surface B 185:110579. https://doi.org/10.1016/j.colsurfb.2019.110579
26. Wei C, Zhang ZZ, Cheng DX et al (2020) An overview of laser-based multiple metallic material additive manufacturing: from macro-to micro-scales. Int J Extrem Manuf 3(1):12003. https://doi.org/10.1088/2631-7990/abce04
27. Feng P, Yang F, Jia JY et al (2024) Mechanism and manufacturing of 4D printing: derived and beyond the combination of 3D printing and shape memory material. Int J Extrem Manuf 6(6):062011. https://doi.org/10.1088/2631-7990/ad7e5f
28. Shuai CJ, Zhao Y, Deng YW et al (2024) Heterogeneous grain structure in biodegradable Zn prepared via mechanical alloying and laser powder bed fusion for strength-plasticity synergy. Virtual Phys Prototy 19(1):e2317780. https://doi.org/10.1080/17452759.2024.2317780
29. Lu JY, Sun M, Zhang JY et al (2023) Benidipine-loaded nanoflower-like magnesium silicate improves bone regeneration. Bio-Des Manuf 6(5):507-521. https://doi.org/10.1007/s42242-023-00240-8
30. Oladapo BI, Zahedi SA, Ismail SO et al (2021) 3D printing of PEEK-cHAp scaffold for medical bone implant. Bio-Des Manuf 4(1):44-59. https://doi.org/10.1007/s42242-020-00098-0
31. Guo WT, Wang XC, Yang CY et al (2022) Microfluidic 3D printing polyhydroxyalkanoates-based bionic skin for wound healing. Mater Futures 1(1):15401.

https://doi.org/10.1088/2752-5724/ac446b

32. Storck JL, Ehrmann G, Uthoff J et al (2022) Investigating inexpensive polymeric 3D printed materials under extreme thermal conditions. Mater Futures 1(1):15001. https://doi.org/10.1088/2752-5724/ac4beb
33. Guo Y, Qiu P, Xu SL et al (2022) Laser-induced microjet-assisted ablation for high-quality microfabrication. Int J Extrem Manuf 4(3):35101. https://doi.org/10.1088/2631-7990/ac6632
34. Yin J, Qian J, Huang Y (2023) Physics problems in bio or bioinspired additive manufacturing. Bio-Des Manuf 6(2):99-102. https://doi.org/10.1007/s42242-023-00234-6
35. Zheng H, Wang SQ, Cheng F et al (2021) Bioactive anti-inflammatory, antibacterial, conductive multifunctional scaffold based on MXene@CeO_2 nanocomposites for infection-impaired skin multimodal therapy. Chem Eng J 424:130148. https://doi.org/10.1016/j.cej.2021.130148
36. Khan SA, Arshad Z, Shahid S et al (2019) Synthesis of TiO_2/graphene oxide nanocomposites for their enhanced photocatalytic activity against methylene blue dye and ciprofloxacin. Compos Part B-Eng 175:107120. https://doi.org/10.1016/j.compositesb.2019.107120
37. Yu HG, Xiao P, Tian J et al (2016) Phenylamine-functionalized rGO/TiO_2 photocatalysts: Spatially separated adsorption sites and tunable photocatalytic selectivity. ACS Appl Mater Interfaces 8(43):29470-29477. https://doi.org/10.1021/acsami.6b09903
38. Gao YF, Yan N, Jiang CX et al (2020) Filtration-enhanced highly efficient photocatalytic degradation with a novel electrospun rGO@TiO_2 nanofibrous membrane: implication for improving photocatalytic efficiency. Appl Catal B-Environ Energy 268:118737. https://doi.org/10.1016/j.apcatb.2020.118737
39. Yang WD, Li YR, Lee YC (2016) Synthesis of r-GO/TiO_2 composites via the UV-assisted photocatalytic reduction of graphene oxide. Appl Surf Sci 380:249-256. https://doi.org/10.1016/j.apsusc.2016.01.118
40. Lee AY, Yang K, Anh ND et al (2021) Raman study of D* band in graphene oxide and its correlation with reduction. Appl Surf Sci 536:147990. https://doi.org/10.1016/j.apsusc.2020.147990

41. Li ZL, Deng LB, Kinloch IA et al (2023) Raman spectroscopy of carbon materials and their composites: graphene, nanotubes and fibres. Prog Mater Sci 135:101089. https://doi.org/10.1016/j.pmatsci.2023.101089
42. Bao HV, Dat NM, Giang NTH et al (2021) Behavior of ZnO-doped TiO_2/rGO nanocomposite for water treatment enhancement. Surf Interface 23:100950. https://doi.org/10.1016/j.surfin.2021.100950
43. Dang XM, Wu S, Zhao HM (2022) Enhanced photocatalytic production of H_2O_2 through regulation of spatial charge transfer and light absorption over a $MnIn_2S_4/WO_3$ (Yb, Tm) Z-scheme system. ACS Sustainable Chem Eng 10(13):4161-4172. https://doi.org/10.1021/acssuschemeng.1c07985
44. Guo W, Zou JH, Guo BB et al (2020) Pd nanoclusters/TiO_2 (B) nanosheets with surface defects toward rapid photocatalytic dehalogenation of polyhalogenated biphenyls under visible light. Appl Catal B Environ 277:119255. https://doi.org/10.1016/j.apcatb.2020.119255
45. Lin Y, Liu XY, Liu ZX et al (2021) Visible-Light-Driven Photocatalysis-Enhanced nanozyme of TiO_2 nanotubes@MoS_2 nanoflowers for efficient wound healing infected with Multidrug-Resistant bacteria. Small 17(39):e2103348. https://doi.org/10.1002/smll.202103348
46. Li XY, Liu YJ, Feng YH et al (2023) Research prospects of graphene-based catalyst for seawater electrolysis. Mater Futures 2(4):042104. https://doi.org/10.1088/2752-5724/acf2fd
47. Bao JF, Li J, Yang YL (2023) Surface-chemistry-mediated near-infrared light-direct-driven photocatalysis toward solar energy conversion: classification and application in energy, environmental, and biological fields. Sol RRL 7(21):2300588. https://doi.org/10.1002/solr.202300588
48. Wang R, Shi MS, Xu FY et al (2020) Graphdiyne-modified TiO_2 nanofibers with osteoinductive and enhanced photocatalytic antibacterial activities to prevent implant infection. Nat Commun 11(1):4465. https://doi.org/10.1038/s41467-020-18267-1
49. Dong BB, Liu TF, Li C et al (2018) Species, engineering and characterizations of defects in TiO_2-based photocatalyst. Chin Chem Lett 29(5):671-680.

https://doi.org/10.1016/j.cclet.2017.12.002

50. Yu WJ, Zou Y, Zhang SN et al (2023) Carbon-based perovskite solar cells with electron and hole-transporting/-blocking layers. Mater Futures 2(2):22101. https://doi.org/10.1088/2752-5724/acbbc2
51. Chen AN, Wang WY, Mao ZY et al (2023) Multimaterial 3D and 4D bioprinting of heterogenous constructs for tissue engineering. Adv Mater:e2307686. https://doi.org/10.1002/adma.202307686
52. Darya V, Konstantin N, Artem V et al (2023) Investigation of the overlapping coefficient impact on the structure and mechanical properties of Al-Mg alloy obtained by wire arc additive manufacturing. J Cent South Univ 30(4):1075-1085. https://doi.org/10.1007/s11771-023-5304-x
53. Bandyopadhyay A, Mitra I, Avila JD et al (2023) Porous metal implants: processing, properties, and challenges. Int J Extrem Manuf 5(3):032014. https://doi.org/10.1088/2631-7990/acdd35
54. Chen AN, Su J, Li YJ et al (2023) 3D/4D printed bio-piezoelectric smart scaffolds for next-generation bone tissue engineering. Int J Extrem Manuf 5(3):032007. https://doi.org/10.1088/2631-7990/acd88f
55. Gu JY, Luo CH, Zhou WF et al (2020) Degradation of Rhodamine B in aqueous solution by laser cavitation. Ultrason Sonochem 68:105181. https://doi.org/10.1016/j.ultsonch.2020.105181
56. Zhao JJ, Guo TY, Wang HT et al (2023) Biobr nanoflakes with engineered thickness for boosted photodegradation of RhB under visible light irradiation. J Alloy Compd 947:169613. https://doi.org/10.1016/j.jallcom.2023.169613
57. Zheng SZ, Du H, Yang LX et al (2023) PDINH bridged NH_2-UiO-66 (Zr) Z-scheme heterojunction for promoted photocatalytic Cr (VI) reduction and antibacterial activity. J Hazard Mater 447:130849. https://doi.org/10.1016/j.jhazmat.2023.130849
58. Mukhtar F, Munawar T, Nadeem MS et al (2022) Highly efficient tri-phase TiO_2-Y_2O_3–V_2O_5 nanocomposite: structural, optical, photocatalyst, and antibacterial studies. J Nanostructure Chem 12:547-564. https://doi.org/10.1007/s40097-021-00430-9
59. Tamang S, Rai S, Bhujel R et al (2023) A concise review on GO, rGO and metal

oxide/rGO composites: fabrication and their supercapacitor and catalytic applications. J Alloy Compd 947:169588. https://doi.org/10.1016/j.jallcom.2023.169588

60. Ziental D, Czarczynska-Goslinska B, Mlynarczyk DT et al (2020) Titanium dioxide nanoparticles: Prospects and applications in medicine. Nanomaterials 10(2):387. https://doi.org/10.3390/nano10020387
61. Bellier N, Baipaywad P, Ryu N et al (2022) Recent biomedical advancements in graphene oxide-and reduced graphene oxide-based nanocomposite nanocarriers. Biomaterials Research 26(1):1-65. https://doi.org/10.1186/s40824-022-00313-2
62. Luo FF, Liu P, Qiu TC et al (2022) Effects of femtosecond laser micropatterning on the surface properties and cellular response of biomedical tantalum-blended composites. J Cent South Univ 29(10):3376-3384. https://doi.org/10.1007/s11771-022-5155-x
63. Zhao DY, Zhu TT, Li J et al (2021) Poly (lactic-co-glycolic acid)-based composite bone-substitute materials. Bioact Mater 6(2):346-360. https://doi.org/10.1016/j.bioactmat.2020.08.016
64. Li GH, Wyatt BC, Song F et al (2021) 2D titanium carbide (MXene) based films: Expanding the frontier of functional film materials. Adv Funct Mater 31(46):2105043. https://doi.org/10.1002/adfm.202105043